

OBSERVATIONS AND MODELING OF THE EMERGING EUV LOOPS IN THE QUIET SUN AS SEEN WITH THE SOLAR DYNAMICS OBSERVATORY

LP. CHITTA^{1,2}, R. KARIYAPPA², A. A. VAN BALLEGOOIJEN¹, E. E. DELUCA¹, S. S. HASAN², AND A. HANSLMEIER³

¹Harvard-Smithsonian Center for Astrophysics, 60 Garden Street MS-15, Cambridge, MA 02138, USA

²Indian Institute of Astrophysics, Bangalore 560 034, India and

³Institut für Physik, IGAM, Universität Graz, Universitätsplatz 5, 8010 Graz, Austria

Draft version October 31, 2018

ABSTRACT

We used data from the Helioseismic and Magnetic Imager (HMI), and Atmospheric Imaging Assembly (AIA) on the *Solar Dynamics Observatory* (SDO) to study coronal loops at small scales, emerging in the quiet Sun. With HMI line-of-sight magnetograms, we derive the integrated and unsigned photospheric magnetic flux at the loop footpoints in the photosphere. These loops are bright in the EUV channels of AIA. Using the six AIA EUV filters, we construct the differential emission measure (DEM) in the temperature range $5.7 - 6.5$ in $\log T$ (K) for several hours of observations. The observed DEMs have a peak distribution around $\log T \approx 6.3$, falling rapidly at higher temperatures. For $\log T < 6.3$, DEMs are comparable to their peak values within an order of magnitude. The emission weighted temperature is calculated, and its time variations are compared with those of magnetic flux. We present two possibilities for explaining the observed DEMs and temperature variations. (a) Assuming the observed loops are comprised of hundred thin strands with certain radius and length, we tested three time-dependent heating models and compared the resulting DEMs and temperatures with the observed quantities. This modeling used Enthalpy-based Thermal Evolution of Loops (EBTEL), a zero-dimensional (0D) hydrodynamic code. The comparisons suggest that a medium frequency heating model with a population of different heating amplitudes can roughly reproduce the observations. (b) We also consider a loop model with steady heating and non-uniform cross-section of the loop along its length, and find that this model can also reproduce the observed DEMs, provided the loop expansion factor $\gamma \sim 5 - 10$. More observational constraints are required to better understand the nature of coronal heating in the short emerging loops on the quiet Sun.

Subject headings: Sun: photosphere — Sun: surface magnetism — Sun: atmosphere — Sun: corona

1. INTRODUCTION

A part of the magnetic field originating in the photospheric sub-surface layers reaches higher up in the solar atmosphere and forms loop like structures, the building blocks of solar corona. These loops harbor plasma, which is heated up to a few million Kelvin, much higher than the photospheric temperature. Finding the source and nature of energy required to heat the corona along with the process of heating is one of the most sought after questions in the field of astrophysics (for reviews on coronal heating, see for example Zirker 1993; Narain & Ulmschneider 1996; Klimchuk 2006; Reale 2010). Studying the dynamics of the plasma filled loops is important to understand the heating mechanisms responsible for these high temperatures. Observational, theoretical, and numerical advances have been made over several decades to understand the physics involved in these processes. Some of the early works on this subject include the ideas of damping of magnetohydrodynamic waves in the lower corona to heat the solar atmosphere (Alfvén 1947, for a recent review on waves in solar corona, see Nakariakov & Verwichte 2005).

From the early x-ray observations (Vaiana et al. 1973), it became evident that the solar corona is confined in the form of loops outlined by the underlying photospheric magnetic field. Later, Rosner et al. (1978), gave an analytical model for the quiescent coronal loops, assuming that these structures are in hydrostatic equilibrium. They suggested that the observations are indicative of

a steady-state heating process. Parker (1988), Cargill (1994), and Cargill & Klimchuk (1997) put forward the idea of intermittent and impulsive (nanoflare) heating, as a viable mechanism. It is now generally believed, and widely accepted that the magnetic field plays an important role in generating and transporting the energy required to maintain the temperatures of the corona. It remains unclear and difficult to identify the dominant process responsible for heating of the solar atmosphere.

As the diagnostics of tenuous coronal plasma improved with the advent of high spatial and temporal resolution space based instruments, an alternate but relevant debate emerged within the community, namely, the frequency of required heating events. The plasma filled in the loops respond to the impulse of heating, and this depends on whether the plasma is reheated before it is completely cooled down (high frequency model — steady heating), or not (low frequency model — nanoflares). Should either of these models operate, they predict certain physical properties of the loops, which can be compared with the observations (see Reale 2010, for a broad review on coronal loop observations and modeling).

With a wide range of field strengths and sizes of magnetic elements, coronal loops also have wide temperature and length distributions. Usually the loops are classified as “hot” ($T > 2 - 3$ MK), and “warm” ($T \approx 1 - 2$ MK) depending on their temperature regime. Both steady and impulsive heating models have been extensively used to explain the observed temperatures,

loop intensity structure e.t.c. Studies indicate that the hot plasma is consistent with both steady heating models (Warren et al. 2010; Winebarger et al. 2011), and impulsive heating models (Tripathi et al. 2010; Viall & Klimchuk 2012). The warm loops are found to be continuously evolving and not in equilibrium (see for example, Ugarte-Urra et al. 2009), and their properties are well explained by impulsive heating models (Spadaro et al. 2003). It is also suggested that the age of an active region might play an important role in determining the dominance of one process over the other (Schmelz & Pathak 2012; Ugarte-Urra & Warren 2012).

The active regions are well studied both in terms of observations and modeling. However, the situation is not so clear in the case of small loops in the quiet Sun. The classification of “hot” and “warm” loops may not be relevant in these features, owing to their compact magnetic structure and narrow temperature range compared to the active regions. These short loops are connected to magnetic bipoles in the photosphere. Their origin can be traced to either flux emergence, or convergence of opposite polarities with reconnection. The magnetic fluxes associated with these regions are typically in the range of $10^{19} - 10^{20}$ Mx. The electron number density in such loops, measured using density sensitive lines is in the order of 10^9 cm^{-3} (Ugarte-Urra et al. 2005; Pérez-Suárez et al. 2008; Doschek et al. 2010).

In this study, we are primarily interested in understanding the nature of the heating that produces the observed 1 – 2 MK temperature in these small bipoles, in particular the frequency of heating events. Also, to better understand the relation between photospheric magnetic field and the coronal loop temperatures, we chose to study emerging flux events. In these events it is easy to identify the loops, and their footpoints in the photosphere. We follow their formation and evolution over many hours. In the following section, we present the observational results. Section 3 describes the loop modeling and the simple heating models we tested in this work. Finally, we summarize the results, and discuss some relevant aspects that require further investigation.

2. OBSERVATIONAL RESULTS

In this section we give a brief note on the datasets used, and present the results derived, namely, the photospheric magnetic flux, and coronal temperatures. The line-of-sight magnetograms observed with the Helioseismic and Magnetic Imager (HMI, Scherrer et al. 2012; Schou et al. 2012), and the intensity images from the EUV channels of Atmospheric Imaging Assembly (AIA, Lemen et al. 2012) are used. HMI and AIA are two of the three instruments onboard *Solar Dynamics Observatory* (SDO, Pesnell et al. 2012). Data are taken from 2011 February 10, and 2012 March 17 observations, spanning for about 12 hr each. SDO observes the full disk of the Sun continuously in different filters with a high cadence of 12 s. We selected a region near disk center with the criteria that, we see emerging magnetic field and coronal loops close to the beginning of the selected time sequence. A few cases of evolved bipoles are also considered.

AIA data contain time sequences from 94 Å, 131 Å, 171 Å, 193 Å, 211 Å, and 335 Å EUV channels. Data are processed with standard procedures available in the

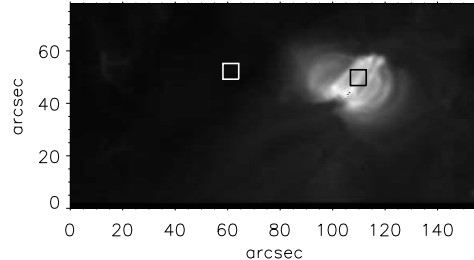


FIG. 1.— A context image showing one of the analyzed bipoles as seen in AIA 193 Å channel. The regions marked with black (near loop top), and white (background region) boxes are used for further analysis to produce DEMs (see Figure 2(a).)

solarsoft library. Alignment between the data from all these channels is crucial. Using 171 Å images as reference, and cross-correlation technique, we aligned all data to within a pixel. The emerging bipoles are identified both in HMI, and AIA. The tracked data cubes of such bipoles are extracted for further analysis. To enhance the signal-to-noise ratio, we prepare the 12 s cadence AIA data to 1 minute cadence by averaging five exposures in each channel. Next, to derive the physical properties of the plasma, we adopt the differential emission measure (DEM), which is related to the electron number density (n_e), and the line-of-sight plasma temperature gradient, and defined as

$$\varphi(T) = n_e^2 \frac{dh}{dT}. \quad (1)$$

We use data from six AIA EUV channels, along with the filter responses¹ as input to construct $\text{DEM}(T)$ ($\text{cm}^{-5} \text{ K}^{-1}$), at each pixel, using `xrt_dem_iterative2.pro` (Golub et al. 2004; Weber et al. 2004, distributed in *solarsoft*). In this program, initial DEM is guessed and folded through the filter responses to generate model observations, which are iteratively used to reduce the χ^2 between the original and modeled observations. This program uses a much tested IDL routine `mpfit.pro` (Markwardt 2009), that performs a Levenberg-Marquardt technique to solve the least-squares problem.

We show results from four emerging bipoles in this work. In Figure 1 we plot the region-of-interest for one of the bipoles analyzed, as seen in AIA 193 Å. The image saturates at 750 DN s^{-1} . For these bipoles, a series of DEMs are constructed near the loop top (for example from a region with in the black box shown in Figure 1) at each pixel in a $6'' \times 6''$ region, over several hours of observations. The predicted intensities from forward modeling of the derived DEMs match the observed intensities with in the limits of errors. Since we restrict the DEMs within a limited range of temperature, the predicted intensities will be lower limits of the observed values. In Figure 2 we plot the average emission from this area as a function of temperature ($\log T$), for all times. Each panel corresponds to a bipole. The dots denote the time dependence. At any given temperature, to show the emission

¹ The filter responses of 94 and 131 Å channels are empirically modified to include contributions from Fe IX and Fe XII for 94 Å, and from Fe VIII and Fe XI for 131 Å. The revised response functions can be obtained using `aia_get_response` with a keyword `chiantifix`, available in *solarsoft*.

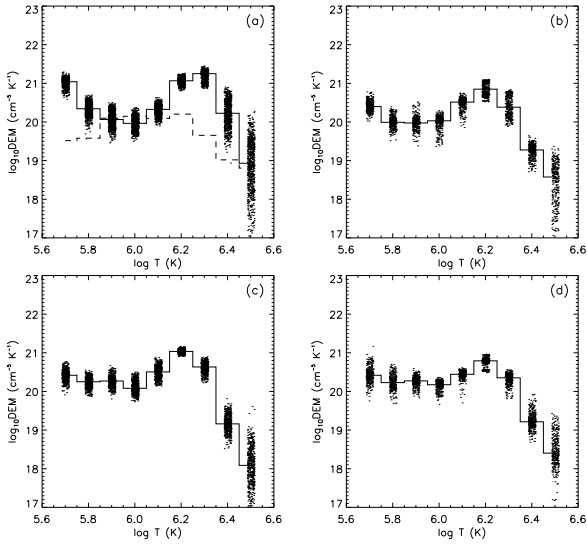


FIG. 2.— DEMs of four bipoles obtained from the observations plotted as a function of temperature for all times (dots). A small offset in temperature is given to the DEMs to show the temporal distribution. Solid line is the temporal median of DEMs obtained for the respective cases. Observed DEMs have a peak around $\log T$ of 6.2 – 6.3. Dashed histogram in panel (a) is the temporal median of five DEMs, at random times, obtained from a *background* region close to the corresponding bipole.

distribution in time, we gave a small offset to DEMs in temperature (and that is the reason we see a small spread of DEMs along $\log T$). Additionally, the temporal distributions also give a sense for the errors in the DEMs. The solid lines are respective temporal medians for all DEMs. They have a peak close to $\log T$ (K) of 6.2 – 6.3. At higher T , they show a rapid decline and also the DEMs are not well constrained. On the other hand, at lower T , the emission stays comparable to the peak emission. Similar results were obtained using *Hinode*/EIS observations, but for a coronal hole bright point (c.f. Fig. 12, Doschek et al. 2010).

We also note that there is no background subtraction to the data in DEM analysis. The small loop structures we analyzed have their loop apex, and footpoints in the same plane along the line-of-sight, much of the emission contribution may be primarily dominated by the loop apex with a part of it originating from the footpoints. To compare the background contribution to the resulting DEMs, for example (a), we considered a 10×10 pixel *background* region adjacent to that bipole (marked with a white box in Figure 1). The DEMs are constructed for this region at five random times, and the temporal median is plotted as a dashed histogram in Figure 2(a). This shows that the observed DEM lies well above the background, not only for $\log T$ in the range 6.2 – 6.4, but also at low temperatures ($\log T \leq 5.8$). The small scatter in the DEM at low T suggest that this emission is real and is not an artifact of the DEM inversion. The DEMs are now used to derive an emission weighted temperature (T_{DEM}) using the relation

$$T_{DEM} = \frac{\sum \{DEM(T_i)T_i\Delta T_i\}}{\sum \{DEM(T_i)\Delta T_i\}}, \quad (2)$$

where $\Delta T_i = 0.1$ in $\log(T)$, is the width of temperature bin around T_i . The time variations of T_{DEM} will be used

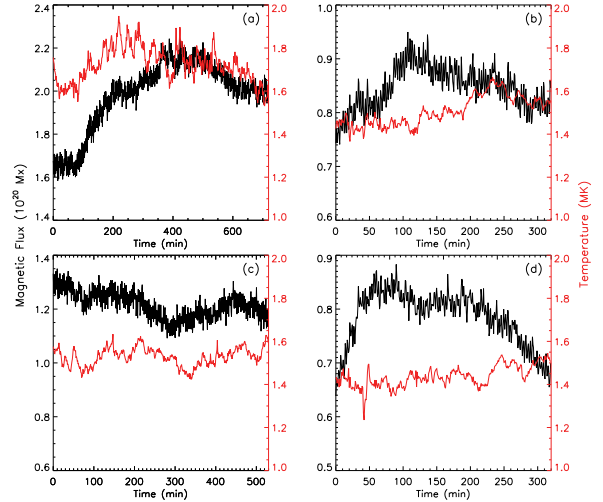


FIG. 3.— Magnetic flux and loop temperatures for a sample of four bipoles. The black curves (left axes) correspond to the integrated photospheric flux density of the bipoles. The red curves (right axes) are the emission weighted, and averaged coronal temperature profiles for the respective bipoles. Panels (a), (b), and (d) are for emerging bipoles, and panel (c) is for an evolved bipole.

later for comparison with loop models.

Integrated unsigned magnetic flux of both polarities associated with these examples, as a function of time, are also calculated from HMI². Such profiles of temperature and magnetic field for a sample of four bipoles are plotted in Figure 3. Three cases of newly emerging bipoles (panels (a), (b), and (d)), and a case of an emerged bipole (panel (c)) are shown. The black curves are time profiles of magnetic flux ($10^{19} - 10^{20}$ Mx), and red curves are temperatures in the range of 1 – 2 MK.

Though they all fall in a category of emerging/ emerged loops, there is no clear relation between the magnetic flux at photosphere and the coronal loop temperature. In other words, it is not trivial to directly relate the field changes in photosphere to the temperature fluctuations in the corona. For example in Figure 3(a), there is a strong correlation between the two physical quantities in the long term trend, but in panel (b) the temperature seem to increase while the flux decreases. In panels (c)-(d), it is more complicated. We suggest that every emerging bipole may behave differently owing to its surrounding structures both in corona and photosphere. However, a common signature is that the temperature fluctuates/ rises at some stage in the emergence process.

To further illustrate this behavior, we consider another example of an emerged bipole. In Figure 4 we plot the magnetic flux (black curve) and temperatures (red curves) this bipole. A sample image of this example from a particular time is also shown above (magnetic structure), and below (coronal loop) the plot. The thin vertical line demarcates the time of snapshot. The solid and dashed red curves are average temperatures derived from two adjacent regions (marked with solid and dashed lines in the image below the plot), of $2''.4 \times 15''$ size each. In the accompanying animation, it is observed that, the drop in temperature after 500 minute is due to the reconnection (in the corona) of the parent bipole with the

² The two polarities are separated by a distance of approximately 10 - 15 Mm in the photosphere.

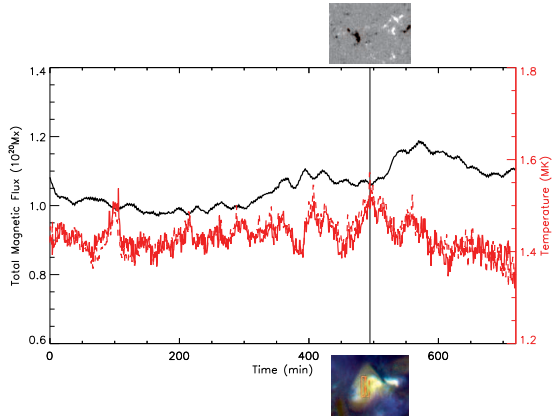


FIG. 4.— Same as in Figure 3. Integrated flux density (black curve), and the temperatures (red solid and dashed curves) of an evolved bipole are plotted. A snapshot of the photospheric field configuration (top image, from HMI, $53'' \times 39''$), and the corresponding coronal loop structure (bottom composite image, from AIA 171 Å, 193 Å, 211 Å channels, $60'' \times 48''$) are shown for a particular time as demarcated by the thin vertical line. The solid and dashed red curves are the emission weighted temperatures derived from 4×25 pixel ($2''.4 \times 15''$) rectangular boxes, from the regions marked in the bottom image respectively. A complete observed evolution of this example is presented as an animation, accompanying this figure.

adjacent opposite polarity regions, changing the topology of the field, and completely disrupting the main loop. Hence the observed temperature of the loops originating from small ephemeral regions possibly depends on various factors.

3. LOOP MODELING

Temperature profile of the loop is a good diagnostic for the loop dynamics but to get a better picture, we also need to estimate the heating rate required to produce the observed temperatures. To this end, we use Enthalpy-based Thermal Evolution of Loops (Klimchuk et al. 2008; Cargill et al. 2012). EBTEL is a time dependent zero-dimensional (0D), hydrodynamic coronal loop model. For a given loop half-length and volumetric heating rate, the code returns the loop properties in terms of average temperature, density, and pressure of the loop and also the values of these quantities at the loop apex (see the Appendix A).

We use EBTEL to model and derive the properties similar to the observed loops (we consider the example shown in Figure 3(a) for this purpose). The properties include the DEM as a function of temperature, and the emission weighted temperature. We compare three different heating scenario and discuss the results. For the models presented in next three subsections we make the following assumptions: (a) A loop is comprised of hundred individual strands, each with a constant length³ of about 18 Mm, and a uniform radius of about 0.1 Mm. In Figure 5 we plot the length and radius of a single strand as a function of time (thick solid and dashed lines, respectively). (b) Each strand is randomly heated with a certain heating profile over a period of 500 minutes. (c) The average values of various physical quantities over all

³ This is only a rough estimate of the length based on the foot-point separation in the photosphere.

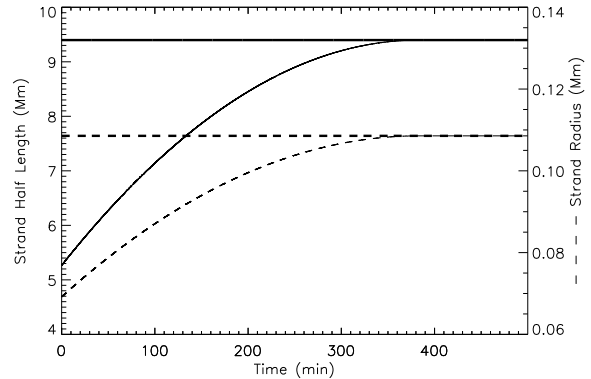


FIG. 5.— Physical dimensions of the strands used in this study. Thick solid and dashed lines, respectively, are the half length and radius of a constant strand. Thin solid and dashed curves, respectively, are the half length and radius of an expanding strand.

the strands, represent the properties of the whole loop. Along with these assumptions, the heating events are chosen such that the modeled emission weighted temperatures closely match the observed temperatures.

In the Section 3.1 we describe the medium frequency heating model. Section 3.2 deals with the low frequency heating model. A medium frequency hybrid heating model is discussed in the Sections 3.3, and 3.4. In Section 3.5 we present an alternate explanation for the observed DEMs by considering a non-uniform cross-section of the loop.

3.1. MEDIUM FREQUENCY HEATING MODEL

In the medium frequency heating model (case 1), individual strands are randomly heated with heating rates having 50 - 100 s temporal fluctuations. These rates are generated by a sequence of random numbers, and further filtering the signal within the desired band of periods. The base or minimum heating rate is 10^{-6} erg cm^{-3} s^{-1} , and the amplitude of the fluctuations vary by up to four orders of magnitude. The average heating rate for a single strand, over the entire duration of 500 minutes is about 4×10^{-3} erg cm^{-3} s^{-1} .

A representative heating rate for one of the strands is plotted in Figure 6(a). The plasma is reheated continuously before it is cooled to the equilibrium temperature due to base heating. In panel (b) we plot the resulting temperature of the strand apex (black, left axis) along with the resulting strand density (red, right axis). The temperature variations are 1 - 3 MK within in a single strand. Panel (c) is the average heating rate of all strands as a function of time. It should be noted that the frequency of this average quantity is not a relevant factor in distinguishing between various heating cases. Similarly in panel (d) we plot the average loop apex temperature (black, left axis), and the average loop density (red, right axis). Since the observed temperatures are derived from weighing the emission distribution, temperature of loop apex in panel (d) cannot be directly compared with its observed counterpart.

In the top panel of Figure 7 we plot the observed DEMs (black dots). The observed DEMs have a broad distribution in temperature with a peak at $\log T$ of 6.3 and another peak at $\log T$ of 5.7 (same as Figure 2(a)). The modeled DEMs, which have a narrow distribution, are

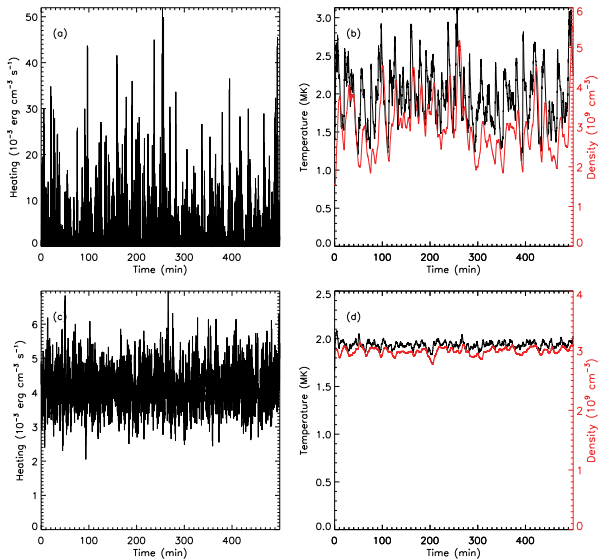


FIG. 6.— Results from a medium frequency heating model (case 1). All the hundred strands are heated with an approximately same average heating rate. (a) A representative input heating given to a single strand with temporal fluctuations of 50 - 100 s. The base heating rate is 10^{-6} erg cm $^{-3}$ s $^{-1}$ for all the strands. The amplitudes of the heating rate fluctuate up to four orders of magnitude. (b) The resulting temperature of the strand apex (black, left axis), and loop density (red, right axis) for the heating profile shown in (a). (c) The average heating rate of hundred random realizations. (d) The average loop apex temperature (black, left axis), and the average loop density (red, right axis) averaged over hundred strands, representing an observed loop.

plotted as red dots with a similar temperature offset. Since there are heating events occurring almost continuously compared to the cooling time of the strands, the loop has no time to cool down completely and the temperature stays steady, with small fluctuations. Because of this reason, all the emission comes from a narrow distribution of temperatures, which is reflected in the modeled results.

Bottom panel is the resulting emission weighted temperatures from observations (black) and modeling (red). Note that the range, and level of fluctuations in the temperature match very well but, modeled DEM has a peak at $\log T$ of 6.25, and the predicted emission about this temperature is at least an order of magnitude more than the observed values. Further, the model predicts a weak or no emission at lower T . By increasing the magnitude of heating rate to match the temperature at which the peak emission occurs, will inherently increase the emission, and also the weighted temperature well beyond the observed T .

3.2. LOW FREQUENCY HEATING MODEL

In the low frequency heating model (case 2), each strand is impulsively heated five times with an average of 100 minutes interval between each impulse. Each triangular pulse has a width of 500 s and a peak input of 10^{-2} erg cm $^{-3}$ s $^{-1}$. Further, the base heating remains the same as in case 1. In Figure 8(a) we plot a sample profile of heat input given to one of the strands. Panel (b) is resulting temperature and density. Note that once the temperature reaches a maximum value, it takes about 70 minutes for the strand to completely cool down.

The average heating rate in panel (c) is less by a fac-

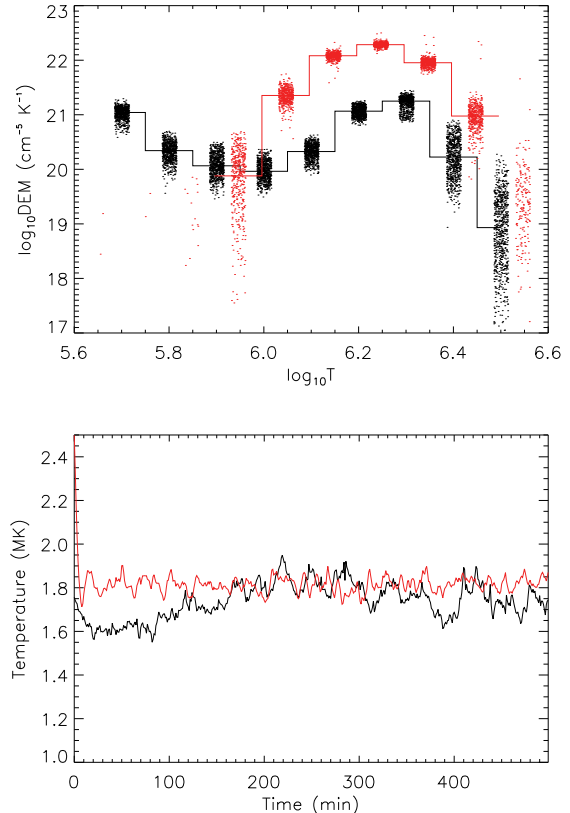


FIG. 7.— Comparison of DEM results obtained for case 1 with the observations. Top panel: DEMs from observations (black dots), and the modeled DEMs (red dots) are shown. All DEMs are given small temperature offsets for a better visualization of the distributions. The black and red solid lines are the temporal medians of observed and modeled DEMs respectively. Bottom panel: Emission weighted temperature derived from observations (black) and modeling (red).

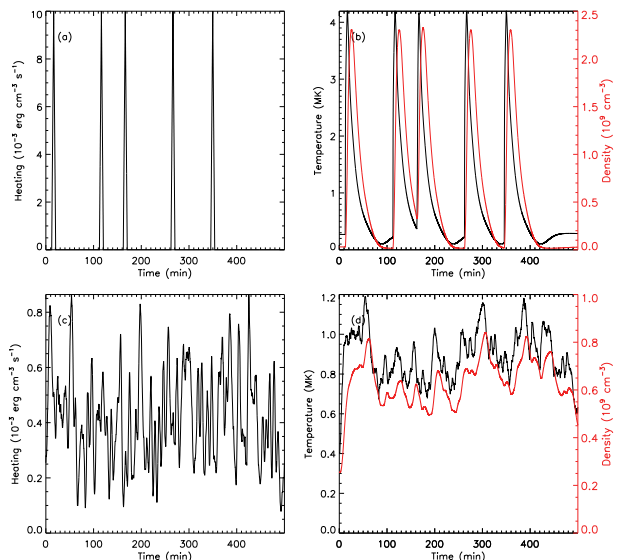


FIG. 8.— Same as Figure 6. Results from a low frequency (impulsive) heating model (case 2). On an average, each strand is heated every 6000 s once, with a triangular heating pulse having a maximum of 10^{-2} erg cm $^{-3}$ s $^{-1}$, and a width of 500 s.

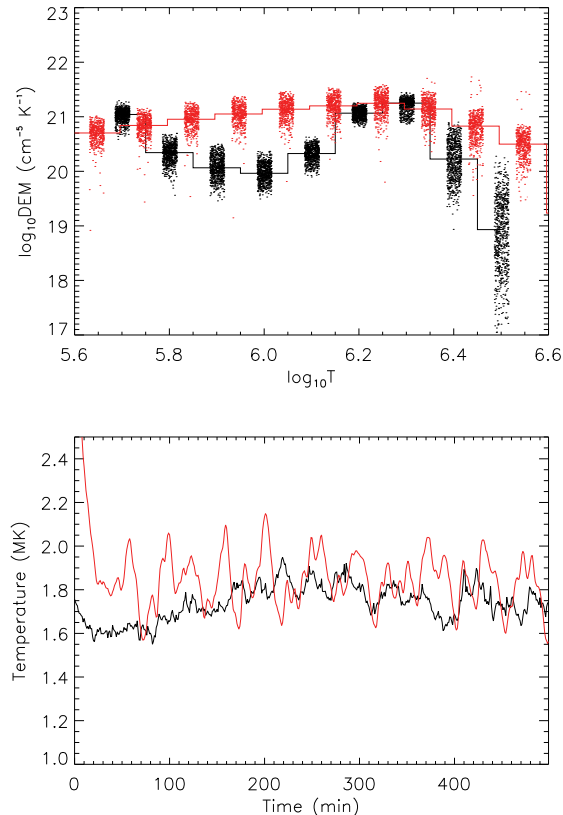


FIG. 9.— Same as Figure 7, but obtained for case 2.

tor of 5 compared to that of case 1. It can be seen that the temperature (panel (b)) in this model has a broad distribution, which is reflected in a very broad DEM distribution shown in Figure 9 (top panel, red). At $\log T$ of 6.5 the model produces a well constrained DEM that is higher than the observed DEM, although the observations are less constrained at those temperatures. Also, the model predicts an overall higher emission at $\log(T) \approx 6.0$

The predicted emission weighted temperature (bottom panel, red) is comparable with observed temperature (bottom panel, black). The level of fluctuations and the short term trend in the red curve are higher than what is seen in the observations. Furthermore, if the number of heating events are fewer than what is considered here (five), but with stronger impulses, the fluctuations now become noticeably large, and the observations should reveal these features.

3.3. MEDIUM FREQUENCY HYBRID HEATING MODEL

For cases 1 and 2 we adjusted the model parameters such that the DEM-weighted temperature (T_{DEM}) roughly matches the observed temperature for region 1. However, we find that the overall structure and features of the predicted DEM(T) does not match the DEM(T) derived from AIA observations. Therefore, neither of these models are fruitful in describing the 1 – 2 MK emerging loops in the quiet Sun. We suggest that the heating events may have a broad range, and/ or a population of different heating amplitudes, influencing differ-

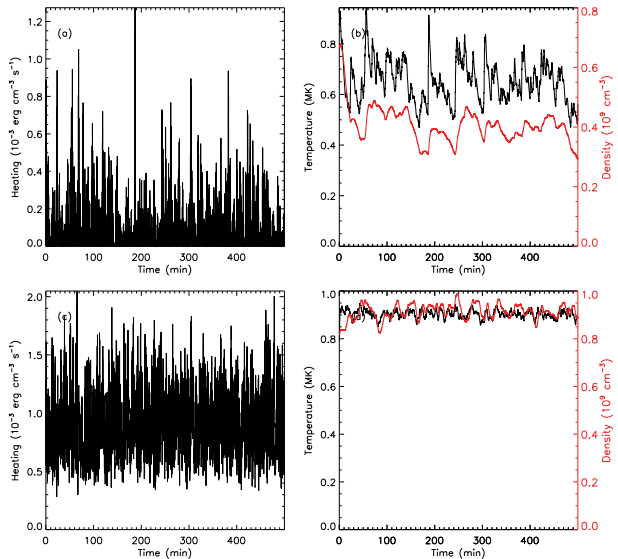


FIG. 10.— Same as Figure 6. Results from a medium frequency hybrid heating model (case 3). 20% of the strands are subjected to higher average heating inputs, but with same temporal fluctuations as in case 1 (see text for details). Shown in panel (a) is an example of lower heating rate case.

ent strands.

From the observational point of view, each strand in the loop is dynamically evolving and the lifetime of this unit is not clearly known. New strands emerge with the photospheric flux and replace the older ones in the loop. To investigate this problem further, a hybrid heating model (case 3) has been considered. In this model, we start with a simple assumption that 20% of the strands are rapidly heated with an excess amount of average heating rate of fifty times more than the remaining 80% of the loops. All loops receive a base heating similar to that of cases 1 and 2.

In Figure 10 we plot the heating rates, temperature, and densities and also the respective average quantities. The profile in panel (a) is a low amplitude heating for a strand in the 80% population. The profiles shown in panel (b) are similar to that of Figure 6(b), except for the overall lower values. Panels (c) and (d) show results averaged over all the strands, including the 20% that receive a higher level of heating. In Figure 11 we show the DEM results for this case. The top panel is for the observed (black) and predicted (red) DEMs. We see that the predicted DEMs now have two distributions, clearly originating from the two populations of heating events. It is interesting to note how closely the observed and predicted DEMs match. The emission weighted temperature is shown in the bottom panel of Figure 11. The fairly well reproduced quantities from this model suggest that a coronal loop, which has a bundle of many strands, can be heated by considering different amplitudes of medium frequency heating events. This is certainly a plausible assumption because, these emerging bipoles evolve continuously, and various reasons can contribute to different heating episodes.

Alternatively, we can also assume that each strand spends 20% of its time being heated to higher values (similar to the 20% strands case described previously), and the remaining time to lower values. Both the sce-

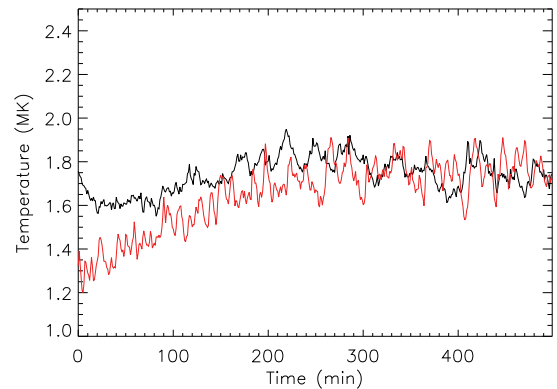
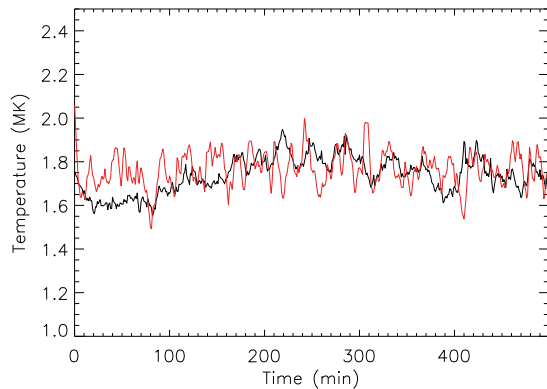
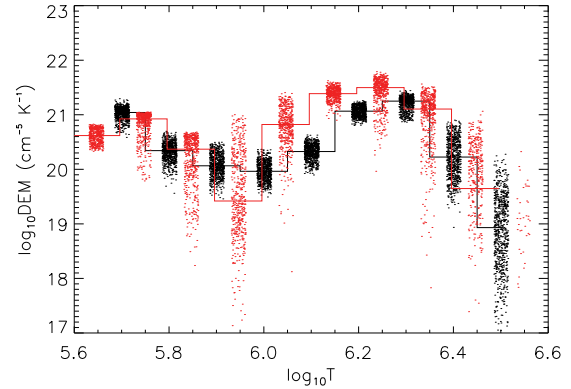
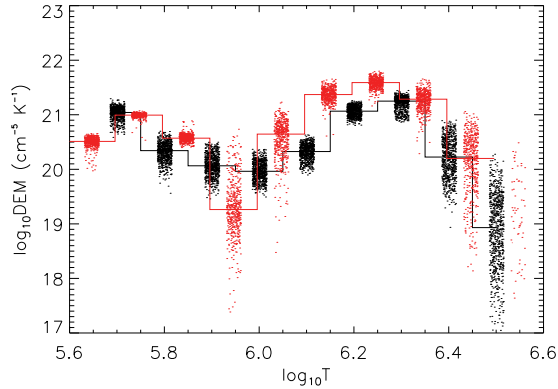


FIG. 11.— Same as Figure 7, but obtained for hybrid heating model (case 3).

FIG. 13.— Hybrid heating model with expanding length and radius as shown in Figure 5 (thin solid and dashed curves respectively). Both the length and radius of the loop vary slowly with time. In this case the temperature (red, lower panel) increases as the length of the loop increases.

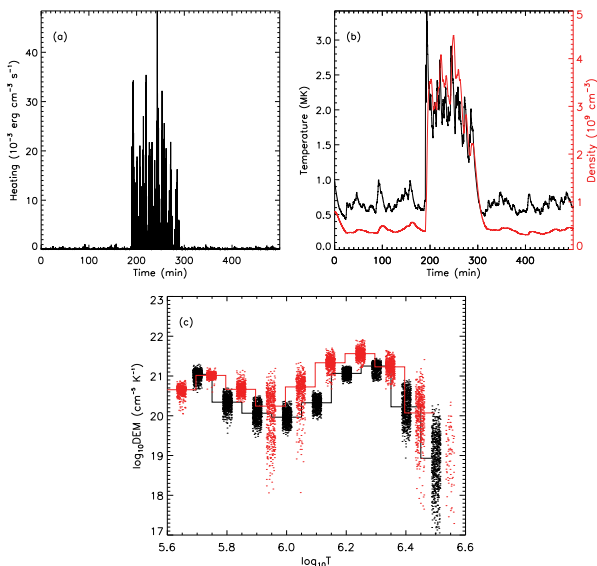


FIG. 12.— Alternative version of case 3 in which, each strand receives high heating events 20% of its time, and the remaining time, low heating events. In panel (a), a sample heating profile is plotted. The panels (b) shows strand apex temperature (black, left axis) and strand density (red, right). The panel (c) is same as the top panel of Figure 11.

narios produce similar results. In Figure 12 we plot the results from this alternative case. The panel (a) is a sample heating profile showing both low and high heating events. In panel (b) the loop apex temperature and density are shown. In panel (c) the observed (black), and predicted (red) DEMs are plotted along with their respective temporal medians.

3.4. A CASE OF EXPANDING LOOP

In general, the coronal loop length increases with time as it emerges through the solar atmosphere. Also, the area as a whole, as the strength of the magnetic field drops with height, the area of strand increases with time. Due to this expansion, filled in plasma may experience additional adiabatic cooling effects, as the loop pressure and density are modified by the volume change (see the Appendix A). We tested heating model described in case 3 on a slowly expanding loop, comprised of hundred strands as explained in the previous sections.

The half length and radius of a single strand are shown as thin solid, and dashed curves in Figure 5. The DEMs and T are plotted in Figure 13. The way we consider the volume expansion is that, each strand slowly expands for about 350 minutes and then the expansion saturates to a constant value. This constant value matches with the length, and radius of the strand chosen in all the cases. It is observed that for a slowly expanding loop, the adiabatic cooling effect can be negligible. There are two

competing effects here. Under equilibrium conditions, the temperature of the loop increases with the length. In our slowly expanding loop, the cooling is compensated for with the length increase. But in reality, the rate of volume expansion can be entirely different, and more rapid than what we considered here. These effects become important when changes in the loop pressure and density due to expansion alone, and heating are comparable.

3.5. EFFECTS OF NON-UNIFORM CROSS-SECTION OF THE LOOP

In the above EBTEL-based models the emission is assumed to come from the coronal portion of the loop. EBTEL also predicts the emission from the transition region (TR) to model the lower temperatures. However, the predicted TR emission is strong and rather flat relative to the corona. Inclusion of up to 5 – 10% of the TR emission will not affect the results, but adding more contribution from the TR requires stronger heating to match the observed emission weighted temperature. This results in a strong emission from the higher temperature, which is not observed.

One possible reason for the strong TR DEMs produced by EBTEL is that the model assumes a constant cross-section over the length of the loop, whereas the loops on the Sun have significant expansion factors (γ) between the loop footpoints in the TR and the loop top in the corona. Potential field modeling of active regions (e.g., Asgari-Targhi & van Ballegooijen 2012) indicates $\gamma = 3 - 30$, depending on height, and similar expansion factors may occur on the quiet Sun. When the cross-sectional area A of a loop increases with height, the volume of plasma at coronal temperatures is increased relative to that at TR temperatures, so the slope of the DEM(T) curve becomes steeper and more consistent with observations.

To demonstrate this effect, we developed a simple loop model for the case that the cross-section A varies along the loop. The heating is assumed to be steady in time. The model is described in Appendix B. It allows us to compute the DEM(T) for a single loop with a given expansion factor γ , half-length L , and peak temperature T_{\max} (we use $L = 9$ Mm). We repeat the calculation for different peak temperatures ($6.0 < \log_{10} T_{\max} < 6.4$) and compute the average DEM(T). In Figure 14 we plot the DEM results for $\gamma = 1$ (left panel) and $\gamma = 5$ (right panel). Note that for a loop with uniform cross-section ($\gamma = 1$), DEM(T) is flat for $T > 10^5$ K, similar to the DEMs predicted with the EBTEL code (see Klimchuk et al. 2008). In contrast, for $\gamma = 5$ the peak value of the DEM in the corona is about 8 times its value in the TR, similar to the observed DEMs (see Figure 2). These results suggest that the overall shape of the observed DEM can be very well reproduced with a collection of hot loops ($T_{\max} > 1$ MK) that have significant expansion factors ($\gamma \sim 5-10$). However, the peak value of the DEM as predicted by the model is larger than the observed value by a factor of about 100. Therefore, the loops must fill only a small fraction of the coronal volume (filling factor $\sim 1\%$).

4. SUMMARY AND DISCUSSION

Using the high temporal cadence observations from the HMI and AIA instruments on board SDO, we studied

the cases of emerging bipolar regions in the quiet Sun. High cadence data from AIA including six EUV channels are re-sampled to 1 minute data to improve the signal-to-noise ratio, as well as, to have a good temporal resolution. Further, `xrt_dem_iterative2.pro` is used to construct DEMs near loop top in a $6'' \times 6''$ pixel region (Section 2, Figure 2). From these DEMs, we get the temporal evolution of emission weighted temperature with Equation (2).

Integrated unsigned magnetic flux derived from the HMI observations ($10^{19} - 10^{20}$ Mx) is compared with the temperature of the loop, for each example (Figure 3). There is no clear relation between the two quantities, suggesting that, for these small emerging bipoles, the surrounding regions in photosphere and higher atmosphere play an important role in the loop evolution.

To estimate the energetics involved in the formation of these loops we use a hydrodynamic loop model (EBTEL) to simulate the DEMs and emission weighted temperatures. We assume that a loop is a bundle of one hundred strands, each having a length of about 18 Mm, and a uniform radius of 0.1 Mm. Furthermore, each strand is randomly heated and the average effect describes the properties of the observed loop. To this end, we tested three simple heating events with varied heating frequencies as described in Sections 3.1, 3.2, 3.3, and 3.4. The average heating input in our study ($\approx 10^6$ ergs $\text{cm}^{-2} \text{s}^{-1}$) is in close agreement with the approximate energy losses observed in the quiet Sun. The 3σ values of the fluctuations in T_{DEM} (MK) are about 0.25, 0.16, 0.55, and 0.24 for the observations, cases 1, 2, and 3(a) respectively.

In case 3, we tested the following sub-cases: (a) 20% of the strands are heated to high heating values all the time, and the remaining strands are heated to low heating values (Section 3.3), (b) all strands are heated to high heating values 20% of their time (Section 3.3), (c) similar to case 3(a), but for expanding strands to account for the adiabatic cooling effects (Section 3.4). It is shown that the cases 3(a), and 3(b) are equivalent and match the observations fairly well. This suggests that there may be a range of heating events operating in the loops at a given time. In the cases 2 and 3(b), though there are only a few large heating events, the essential difference between the two cases is that, unlike in case 2, the duration of a single high heating phase in case 3(b) itself is longer compared to typical plasma cooling time (making case 3(b) statistically a steady heating model). This allows case 3(b) to find a DEM peak at higher temperatures. The model described in case 3 is the best model we could obtain with in the scope of the present work. Mixing low and medium heating at various proportions with different average heating rates show discrepancy, and do not fit observations completely. These results are based on the assumption that the emitting plasma has coronal origin.

Alternatively, we also argued that to include TR emission in the model, it is important to consider an expansion of the loop from TR to corona. In this scenario, a steady heating model for loops with loop apex temperature $> 10^6$ K can well reproduce the observed DEMs, assuming $\sim 1\%$ plasma filling factor.

Reliability of AIA DEMs is a matter of debate. O'Dwyer et al. (2010) studied the contribution of spectral lines and continuum emission to the AIA EUV channels using CHIANTI atomic database. They em-

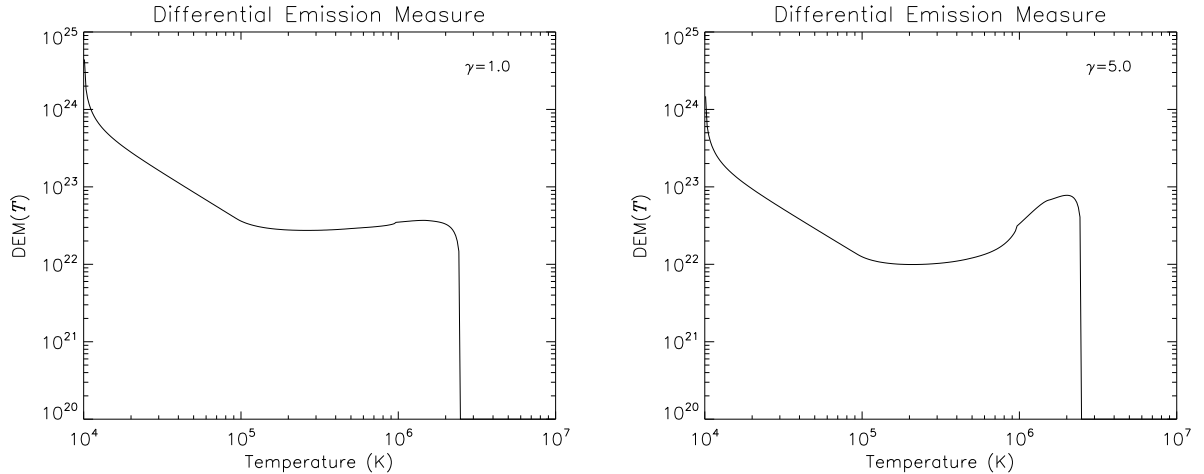


FIG. 14.— Results from a simple loop model assuming steady heating. Left panel: DEM of a loop with expansion factor (γ) = 1. Note the flat DEM in the range of $10^5 < T(\text{K}) < 10^6$. Right panel: Similar to the left panel, but with $\gamma = 5$. The DEM now shows a clear peak at $T \approx 2$ MK.

phasize that the contribution of particular spectral lines and continuum emission can affect the interpretation of the observed features, when AIA channels are used to observe regions other than those for which the channels were designed. Del Zanna et al. (2011) compared AIA DEMs with the *Hinode*/EIS observations of active regions. They found discrepancies between the derived DEMs. This is mainly due to the multi-thermal nature of AIA response curves, which have contributions from cooler components. The cooler emission below 6.0 (in $\log T$), seen in our observations could be due to the double-peaked nature of AIA responses as suggested by Del Zanna et al. (2011). Empirically modified filter response curves for AIA are derived to address some of these issues however, the role of this possible contamination in a already cool loop (like the one originating from a small bipole in the quiet Sun), as compared to the warm loops in the hotter active region has to be further examined.

The models presented in this work assume that the strands are heated uniformly over their entire length. Alternatively, the strand can be heated in a non-uniform manner with localized and concentrated heat sources. If the heating is concentrated at the loop footpoints, this may lead to the loss of equilibrium in the energy balancing terms, as the radiative losses in the coronal section dominate the downward conductive flux. This will trigger the runaway cooling due to strong radiative losses and a condensation is formed in the coronal loops (for example Hood & Priest 1980; Müller et al. 2004). This is a well studied phenomenon in the formation of solar prominences (Antiochos & Klimchuk 1991; Antiochos et al. 1999). Recently, based upon the observed properties of the hot, and warm loops in active regions, Klimchuk et al. (2010) have argued that the high concentration of heating low in the corona, and the steady or quasi-steady heating models (leading to thermal nonequilibrium) can be ruled out. However, Peter et al. (2012) claim that a steady supply of energy is required even in the events of condensation in the corona, to keep the coronal pressure. They also suggested that thermal non-equilibrium can be a valuable tool in investigating the plasma dynamics and heat input in the

regions where condensation forms.

The studies on the role and importance of the thermal non-equilibrium in the formation of condensation in the short quiet Sun loops are not extensive. Müller et al. (2003), Müller et al. (2004) discussed in detail the numerical simulations of condensation and catastrophic cooling of short TR 10 Mm loops, and longer 100 Mm coronal loops, respectively. They considered heating that has exponential height dependence along the loop, and further suggested that the catastrophic cooling is initiated by the loss of equilibrium at the loop apex due to concentration of heating at the footpoints, but not due to a drastic decrease of the total loop heating.

Note that the strands in a loop may interact in a very complex manner, and their response to the condensation is the key objective to be addressed. Further work is necessary to get a better picture of the nature and location of the heating, observational signatures of condensation, and finally the role of magnetic field in this whole process. A complete set of answers for these questions is still elusive and we need more observational constraints to narrow down the possibilities.

The authors thank the referee for many comments and suggestions that helped in improving the presentation of the manuscript. LPC is a 2011 – 2013 SAO Pre-Doctoral Fellow at the Harvard-Smithsonian Center for Astrophysics. Funding for LPC and EED is provided by NASA contract NNM07AB07C. Funding from the Indo-Austria exchange program (INT/AUA/BMWF/P-11/2011) is acknowledged. LPC thanks Jim Klimchuk, Steve Saar, and Mark Weber for many useful suggestions and discussions. Courtesy of NASA/SDO and the AIA and HMI science teams. This research has made use of NASA’s Astrophysics Data System.

APPENDIX

EBTEL AND LOOPS THAT EXPAND WITH TIME

The standard version of EBTEL assumes a symmetric loop with constant loop length and, uniform cross-section. The model is based on the 1D time-dependent energy conservation equation

$$\frac{\partial E}{\partial t} = -\frac{\partial}{\partial s}v(E + P) - \frac{\partial F_c}{\partial s} + Q - n^2\Lambda(T), \quad (\text{A1})$$

where s is a spatial coordinate along the magnetic field; $E = \frac{3}{2}P + \frac{1}{2}\rho v^2$ is the total energy density; n, T, P , and v are the electron number density, temperature, total pressure, and plasma bulk velocity, respectively; F_c is the heat flux; Q is volumetric heating rate; and $\Lambda(T)$ is the radiative loss function for optically thin plasma. It is assumed that the velocity and heat flux both vanish at the loop apex due to symmetry. Also, the flow velocity is subsonic, and gravity is neglected in the energy equation. Integrating the above equation over the coronal (L), and TR (l) lengths with the above assumption, we get

$$\frac{3}{2}L\frac{\partial \bar{P}}{\partial t} \approx \frac{5}{2}P_0v_0 + F_0 + L\bar{Q} - \mathcal{R}_c, \quad (\text{A2})$$

$$\frac{3}{2}l\frac{\partial \bar{P}_{tr}}{\partial t} \approx -\frac{5}{2}P_0v_0 - F_0 + l\bar{Q}_{tr} - \mathcal{R}_{tr}, \quad (\text{A3})$$

where overbar denotes the spatial averages of the quantities over respective sections of the loop, and subscript 0 denotes the values at the base of the corona; \mathcal{R}_c , and \mathcal{R}_{tr} are the coronal, and the TR radiative loss rates respectively. Neglecting the terms involving l (for a thin TR), and together with ideal gas law⁴, \bar{P} and \bar{n} can be approximated⁵ with

$$\frac{d\bar{P}}{dt} \approx \frac{2}{3} \left[\bar{Q} - \frac{1}{L}(\mathcal{R}_c + \mathcal{R}_{tr}) \right], \quad (\text{A4})$$

$$\frac{d\bar{n}}{dt} \approx -\frac{1}{5kLT_0} (F_0 + \mathcal{R}_{tr}). \quad (\text{A5})$$

For a given heating rate $\bar{Q}(t)$, the EBTEL model returns \bar{P}, \bar{n} , and \bar{T} , with other useful quantities.

For a uniformly expanding strand of length $L(t)$ and radius $R(t)$ adiabatically, the above equations are modified by adding a term $-\gamma\bar{P}\xi(t)$ on the right hand side of Equation (A4), and $-\bar{n}\xi(t)$ in Equation (A5), where $\gamma = 5/3$ is the ratio of specific heats, and

$$\xi(t) = \frac{1}{L} \frac{dL}{dt} + \frac{2}{R} \frac{dR}{dt}. \quad (\text{A6})$$

The strand pressure, density, and temperature are modeled accordingly. The time varying length and radius of a single strand are shown as thin solid and dashed curves, respectively, in Figure 5. Note that $R(t)$ explicitly enters the scheme only through Equation (A6), and everywhere else, it is absorbed due to volumetric averaging.

MODEL FOR LOOPS THAT EXPAND WITH HEIGHT

In this section we describe a loop model for the case that the cross-sectional area A varies along the loop. For simplicity the area $A(T)$ is considered to be a function of temperature:

$$A(T) = \exp \left\{ \ln \gamma \left[\frac{z(T)}{z(T_{\max})} - 1 \right] \right\}, \quad (\text{B1})$$

where T_{\max} is the maximum temperature at loop top, and $z(T)$ is a monotonically increasing function, starting with $z \approx 0$ at the base of the TR. We use $z(T) = y + \sqrt{1 + y^2}$ with $y = (x - x_0)/x_1$ and $x = \log_{10} T$. The constants x_0 and x_1 are set to 6.0 and 0.2, respectively, so that most of the area change occurs near a temperature of 1 MK. Similarly, the volumetric heating rate is

$$Q(T) = Q_{\max} \left(\frac{T}{T_{\max}} \right)^m, \quad (\text{B2})$$

where Q_{\max} is the heating rate at the loop top, and m is an exponent (for the models presented here we set $m = 0$). The loop is assumed to be symmetric, and heating is assumed to be steady in time. We solve the following energy balance equation:

$$\frac{\partial}{\partial s} (AF_c) = A(T) [Q(T) - n^2\Lambda(T)], \quad (\text{B3})$$

⁴ $P = 2nkT$, where k is the Boltzmann's constant.

⁵ simple volumetric averaging yields similar results.

where s is a spatial coordinate along the magnetic field, $F_c(s) \equiv -\kappa_0 T^{5/2} \partial T / \partial s$ is the conductive heat flux, $n(s)$ is the electron density, and $\Lambda(T)$ is the radiative loss function, which is taken from Klimchuk et al. (2008). Multiplying equation (B3) by $A F_c$ and integrating over position along the loop, we obtain:

$$\frac{1}{2} A^2 F_c^2 = \kappa_0 Q_{\max} [f E_1(T) - E_2(T)], \quad (\text{B4})$$

where

$$E_1(T) = \int_{T_{\text{base}}}^T A^2(T) \Lambda(T) T^{1/2} dT, \quad (\text{B5})$$

$$E_2(T) = \int_{T_{\text{base}}}^T A^2(T) (T/T_{\max})^m T^{5/2} dT. \quad (\text{B6})$$

Here T_{base} is the temperature at the base of the TR ($T_{\text{base}} = 10^4$ K), and we assume $F_c = 0$ at the base. The factor f is given by

$$f \equiv \frac{P^2}{4k^2 Q_{\max}} = \frac{E_2(T_{\max})}{E_1(T_{\max})}, \quad (\text{B7})$$

where $P = 2nkT$ is the plasma pressure (a constant), and the last equality in (B7) follows from the requirement that $F_c = 0$ at the loop top. Then the loop half-length L is given by

$$L = \int_{s_{\text{base}}}^{s_{\text{max}}} ds = \left(\frac{\kappa_0}{2Q_{\max}} \right)^{1/2} \int_{T_{\text{base}}}^{T_{\max}} \frac{A(T) T^{5/2} dT}{\sqrt{f E_1(T) - E_2(T)}}. \quad (\text{B8})$$

For a given peak temperature T_{\max} and half-length L , we can compute the heating rate Q_{\max} , pressure P , heat flux $F_c(T)$, and density $n(T)$. Then the DEM is given by $\varphi(T) = n^2(T) A(T) (\partial T / \partial s)^{-1}$. Since the area factor is normalized such that $A(T_{\max}) = 1$, this DEM(T) does not include the effects of a possible filling factor of the coronal loops.

REFERENCES

- Alfvén, H. 1947, MNRAS, 107, 211
 Antiochos, S. K., & Klimchuk, J. A. 1991, ApJ, 378, 372
 Antiochos, S. K., MacNeice, P. J., Spicer, D. S., & Klimchuk, J. A. 1999, ApJ, 512, 985
 Asgari-Targhi, M., & van Ballegooijen, A. A. 2012, ApJ, 746, 81
 Cargill, P. J. 1994, ApJ, 422, 381
 Cargill, P. J., Bradshaw, S. J., & Klimchuk, J. A. 2012, ApJ, 752, 161
 Cargill, P. J., & Klimchuk, J. A. 1997, ApJ, 478, 799
 Del Zanna, G., O'Dwyer, B., & Mason, H. E. 2011, A&A, 535, A46
 Doschek, G. A., Landi, E., Warren, H. P., & Harra, L. K. 2010, ApJ, 710, 1806
 Golub, L., Deluca, E. E., Sette, A., & Weber, M. 2004, in Astronomical Society of the Pacific Conference Series, Vol. 325, The Solar-B Mission and the Forefront of Solar Physics, ed. T. Sakurai & T. Sekii, 217
 Hood, A. W., & Priest, E. R. 1980, A&A, 87, 126
 Klimchuk, J. A. 2006, Sol. Phys., 234, 41
 Klimchuk, J. A., Karpen, J. T., & Antiochos, S. K. 2010, ApJ, 714, 1239
 Klimchuk, J. A., Patsourakos, S., & Cargill, P. J. 2008, ApJ, 682, 1351
 Lemen, J. R., et al. 2012, Sol. Phys., 275, 17
 Markwardt, C. B. 2009, in Astronomical Society of the Pacific Conference Series, Vol. 411, Astronomical Data Analysis Software and Systems XVIII, ed. D. A. Bohlender, D. Durand, & P. Dowler, 251
 Müller, D. A. N., Hansteen, V. H., & Peter, H. 2003, A&A, 411, 605
 Müller, D. A. N., Peter, H., & Hansteen, V. H. 2004, A&A, 424, 289
 Nakariakov, V. M., & Verwichte, E. 2005, Living Reviews in Solar Physics, 2, 3
 Narain, U., & Ulmschneider, P. 1996, Space Sci. Rev., 75, 453
 O'Dwyer, B., Del Zanna, G., Mason, H. E., Weber, M. A., & Tripathi, D. 2010, A&A, 521, A21
 Parker, E. N. 1988, ApJ, 330, 474
 Pérez-Suárez, D., Maclean, R. C., Doyle, J. G., & Madjarska, M. S. 2008, A&A, 492, 575
 Pesnell, W. D., Thompson, B. J., & Chamberlin, P. C. 2012, Sol. Phys., 275, 3
 Peter, H., Bingert, S., & Kamio, S. 2012, A&A, 537, A152
 Reale, F. 2010, Living Reviews in Solar Physics, 7, 5
 Rosner, R., Tucker, W. H., & Vaiana, G. S. 1978, ApJ, 220, 643
 Scherrer, P. H., et al. 2012, Sol. Phys., 275, 207
 Schmelz, J. T., & Pathak, S. 2012, ApJ, 756, 126
 Schou, J., et al. 2012, Sol. Phys., 275, 229
 Spadaro, D., Lanza, A. F., Lanzafame, A. C., Karpen, J. T., Antiochos, S. K., Klimchuk, J. A., & MacNeice, P. J. 2003, ApJ, 582, 486
 Tripathi, D., Mason, H. E., & Klimchuk, J. A. 2010, ApJ, 723, 713
 Ugarte-Urra, I., Doyle, J. G., & Del Zanna, G. 2005, A&A, 435, 1169
 Ugarte-Urra, I., & Warren, H. P. 2012, ApJ, 761, 21
 Ugarte-Urra, I., Warren, H. P., & Brooks, D. H. 2009, ApJ, 695, 642
 Vaiana, G. S., Krieger, A. S., & Timothy, A. F. 1973, Sol. Phys., 32, 81
 Viall, N. M., & Klimchuk, J. A. 2012, ApJ, 753, 35
 Warren, H. P., Winebarger, A. R., & Brooks, D. H. 2010, ApJ, 711, 228
 Weber, M. A., Deluca, E. E., Golub, L., & Sette, A. L. 2004, in IAU Symposium, Vol. 223, Multi-Wavelength Investigations of Solar Activity, ed. A. V. Stepanov, E. E. Benevolenskaya, & A. G. Kosovichev, 321–328
 Winebarger, A. R., Schmelz, J. T., Warren, H. P., Saar, S. H., & Kashyap, V. L. 2011, ApJ, 740, 2
 Zirker, J. B. 1993, Sol. Phys., 148, 43